ACS Partner Journal

CHEMICAL & BIOMEDICAL IMAGING

pubs.acs.org/ChemBioImaging

Article

Multimodal Imaging Unveils the Impact of Nanotopography on Cellular Metabolic Activities

Zhi Li,[#] Einollah Sarikhani,[#] Sirasit Prayotamornkul, Dhivya Pushpa Meganathan, Zeinab Jahed,[*] and Lingyan Shi[*]

Cite This: *Chem. Biomed. Imaging* 2024, 2, 825−834

Read Online

ACCESS | Metrics & More | Article Recommendations | Supporting Information

ABSTRACT: Nanoscale surface topography is an effective approach in modulating cell-material interactions, significantly impacting cellular and nuclear morphologies, as well as their functionality. However, the adaptive changes in cellular metabolism induced by the mechanical and geometrical microenvironment of the nanotopography remain poorly understood. In this study, we investigated the metabolic activities in cells cultured on engineered nanopillar substrates by using a label-free multimodal optical imaging platform. This multimodal imaging platform, integrating two photon fluorescence (TPF) and stimulated Raman scattering (SRS) microscopy, allowed us to directly visualize and quantify metabolic activities of cells in 3D at the subcellular scale. We discovered that the nanopillar structure significantly reduced the cell spreading area and circularity compared to flat surfaces. Nanopillar-induced mechanical cues significantly modulate cellular metabolic activities with variations in nanopillar geometry further influencing these metabolic processes. Cells cultured on nanopillars exhibited reduced oxidative stress, decreased protein and lipid synthesis, and lower lipid unsaturation in comparison to those on flat substrates. Hierarchical clustering also revealed that pitch differences in the nanopillar had a more significant impact on cell metabolic activity than diameter variations. These insights improve our understanding of how engineered nanotopographies can be used to control cellular metabolism, offering possibilities for designing advanced cell culture platforms which can modulate cell behaviors and mimic natural cellular environment and optimize cell-based applications. By leveraging the unique metabolic effects of nanopillar arrays, one can develop more effective strategies for directing the fate of cells, enhancing the performance of cell-based therapies, and creating regenerative medicine applications.

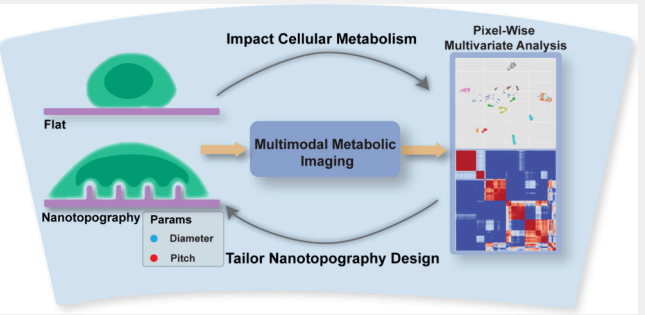

KEYWORDS: *Nanotopography, Nanopillar, Cell metabolism, Metabolic dynamics, Multimodal imaging, Multivariate analysis, Unsupervised clustering*

INTRODUCTION

Engineered nanoscale surface topography has demonstrated significant potential in modulating cell-material interactions by offering distinct physical cues to which cells respond.[1−4] It can effectively guide the interaction between materials and biological systems, mimicking natural structures such as viral spike proteins.[5,6] Nanopillar arrays consist of repeating patterns of freestanding cylinders, usually with diameters measuring a few hundred nanometers. These nanopillar arrays are notable for their high surface area-to-volume ratio, biocompatibility, and precise control over their geometry and material composition.[7,8] Because of these beneficial properties, nanopillar platforms are being developed for various fundamental research purposes and clinical applications in the biomedical field.[9] Recent studies have employed nanopillar arrays for a variety of purposes, including biomolecule delivery, development of advanced nanobioelectronics for neuronal and cardiac electrophysiology,[10−13] and cancer malignancy detection platforms.[14]

Previous studies have shown that cells cultured on nanopillar arrays exhibit markedly altered behaviors compared to those grown on flat substrates, and the physical structure of nanotopography can greatly impact cellular growth, adhesion, proliferation and differentiation.[15−19] It is crucial to understand these physical alterations for optimizing the design and application of nanotopographic materials in biomedical contexts.[20−22] Numerous studies have shown that nanopillars can alter cell and nuclear biophysical properties such as the stiffness and spreading area.[23,24] However, the impact of nanopillars on cellular metabolism has been less explored. Understanding this has far reaching implications for the

Received: July 14, 2024
Revised: November 1, 2024
Accepted: November 4, 2024
Published: November 18, 2024

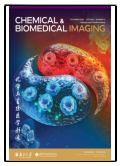

https://doi.org/10.1021/cbmi.4c00051
Chem. Biomed. Imaging 2024, 2, 825−834

development of new biomedical technologies. For example, modulating cellular metabolism through engineered surfaces could enhance the efficacy of cell based therapies, improve the design of drug delivery systems, and lead to novel approaches for tissue engineering.[25]

Optical imaging technologies provide direct, noninvasive means for investigating the metabolic activities of cells. We have developed a multimodal optical imaging platform, combining two-photon fluorescence (TPF) microscopy and stimulated Raman scattering (SRS) microscopy, for visualizing cellular metabolic activities *in situ* at the subcellular level.[26,27] TPF microscopy allows for high resolution deep tissue imaging, and more importantly, for evaluating cellular metabolism via autofluorescence imaging of autofluorescent biomolecules such as reduced nicotinamide adenine dinucleotide (NADH) and flavin adenine dinucleotide (FAD).[26,28,29] SRS microscopy enables the imaging of various biomolecules (lipids, protein, etc.) based on their vibrational chemical bonds.[30−32] Combined with heavy water (D_2O) labeling, SRS can further visualize metabolic dynamics of biomolecules in cells and tissues.[33]

In this study, we employed a novel multimodal optical imaging platform combining TPF and SRS microscopy to investigate the effects of nanopillar arrays on cellular metabolism. Our findings revealed that nanopillar structures not only altered cellular and nuclear morphologies but also significantly influenced key metabolic processes. Specifically, we observed that cells cultured on nanopillars exhibited reduced oxidative stress, decreased protein and lipid synthesis, and lower lipid unsaturation compared with those on flat substrates. Through multivariate analysis, we identified distinct metabolic profiles that clearly distinguished cells on nanopillar surfaces from those on flat surfaces. Importantly, we found that variations in nanopillar geometry, particularly the interpillar spacing, had a more significant impact on cellular metabolic activity than diameter differences. These insights enhance our understanding of how engineered nanotopographies can be used to control cellular metabolism and offer new possibilities for designing advanced cell culture platforms and optimizing cell-based applications in fields such as regenerative medicine and drug development.

MATERIALS AND METHODS

Nanopillar Fabrication

Nanopillar chips were fabricated on a 4 in. fused quartz wafer. The wafers underwent RCA cleaning using SC1 and SC3 solutions followed by spin rinsing and drying. AZ 1512 photoresist was then spin-coated at 4000 rpm for 45 s, achieving a thickness of approximately 1.2 μm. Using a custom design file, the wafers were patterned and exposed with a Heidelberg MLA system at 375 nm with a dosage of 300. After patterning, the substrates were developed with AZ400 developer for 30 s. Chromium (Cr) was deposited via an electron beam evaporator. A lift-off process using RR41, acetone, and isopropyl alcohol (IPA) followed, removing excess photoresist.

The substrates were etched for 50 min using reactive ion etching (RIE) with argon (35 sccm) and chlorotrifluoromethane (25 sccm) under conditions of 50 mT and 200 W. Subsequently, the wafers were wet etched in a chromium etchant and then in a buffered oxide etch (BOE) to remove the exposed quartz. Finally, the wafers were diced into 1 cm × 1 cm chips for further preparation, and three different configurations of nanopillars were tested with different diameter (d) and pitch (p) sizes, d1p2.5 (diameter 1 μm, pitch 2.5 μm), d1p3.5, and d2p4.5.

Nanopillar Preparation

Nanopillar chips were prepared for cell seeding following a previously described protocol. In brief, the chips were sterilized and then washed sequentially with ethanol and deionized (DI) water.[34,35] After being washed, they were air-dried. The dried chips were then subjected to ultraviolet ozone (UVO) treatment for 10 min to clean the surface.

Following UVO treatment, the chips were incubated with a 0.1 mg/mL poly-L-lysine (PLL) solution for 30 min at room temperature. After incubation, the chips were washed with DI water and subsequently treated with a 0.5% glutaraldehyde solution, followed by another incubation with the 0.1 mg/mL gelatin solution for 30 min each. After these treatments, the chips were washed again with DI water and stored in phosphate-buffered saline (PBS) until they were ready for cell seeding.

Cell Culture and Seeding

HeLa cells (ATCC) were cultured in Dulbecco's Modified Eagle Medium (DMEM, Gibco, USA) supplemented with 10% fetal bovine serum (FBS, Sigma-Aldrich, USA) and 1% penicillin-streptomycin (P/S, Sigma-Aldrich, USA). Cells were detached using TrypLE Express Enzyme (1X) (Gibco, USA). Following detachment, the cells were centrifuged and the supernatant was removed to obtain a cell pellet. This pellet was then resuspended in fresh DMEM.

For the media containing D_2O, 10 mg of DMEM powder was mixed with 4.7 mL of Milli-Q water (H_2O). Then, 4.7 mL of D_2O was added to the culture medium along with 0.5 mL of fetal bovine serum (5% FBS), and 0.1 mL of penicillin/streptomycin (1% P/S). The solution was thoroughly mixed via vortex.

The cells were maintained in the incubator at 37 °C with 5% CO_2. For cell seeding, a droplet containing 50,000 cells was carefully added to each nanopillar chip. The chips were then incubated at 37 °C for 8 h to allow the cells to fully attach and spread on the surface. Cells were fixed with 4% paraformaldehyde (Electron Microscopy Sciences, USA) for 10 min at room temperature, followed by three washes with PBS. Next, the cells were permeabilized with 0.1% Triton X-100 (Sigma-Aldrich, USA) for 10 min at room temperature and washed three times with PBS. Samples were then incubated for 5 min with 4′,6-diamidino-2-phenylindole (DAPI) (Thermo Scientific, USA) for nuclear staining, followed by a 20 min incubation with Alexa 594-phalloidin (Invitrogen, USA) at room temperature for actin staining.

Shape Analysis Method. Images were captured using an Echo Revolve microscope equipped with a 20× Plan Fluorite objective. Fluorescent image analysis and morphology measurements were conducted using ImageJ 1.53 (NIH, US). The area, perimeter, and circularity of the objects were calculated using the "Analyze Particles" command in ImageJ. Circularity was computed using the following formula:

$$\text{Circularity} = \frac{4 \times \pi \times \text{Area}}{\text{Perimeter}^2}$$

Label-Free Multimodal Optical Imaging

An upright laser-scanning microscope (DIY multiphoton, Olympus) with a 25x water objective (XLPLN, WMP2, 1.05 NA, Olympus) was utilized for near-IR throughput. Synchronized pulsed pump beam (tunable 780−990 nm wavelength, 5−6 ps pulse width, and 80 MHz repetition rate) and Stokes beam (wavelength at 1031 nm, 6 ps pulse width, and 80 MHz repetition rate) were supplied by a picoEmerald system (Applied Physics & Electronics) and coupled into the microscope. The pump and Stokes beams were collected in transmission by a high NA oil condenser (1.4 NA). In two photon fluorescence (TPF) mode, pump laser beam at 781 and 860 nm were used to excite reduced nicotinamide adenine dinucleotide (NADH) and flavin adenine dinucleotide (FAD) molecules, respectively. The related filters for NADH and FAD are 460 ± 10 *nm* and 515 ± 10 *nm* nm. All images obtained were 512 × 512 pixels, with a dwell time 8 μs and average 2. In SRS mode, the fixed Stokes beam and a tunable pump laser were used. A high optical density (O.D.) short-pass filter (950 nm, Thorlabs) was used to completely block the Stokes beam and only allowed the pump beam into a Si photodiode for the

https://doi.org/10.1021/cbmi.4c00051
Chem. Biomed. Imaging 2024, 2, 825−834

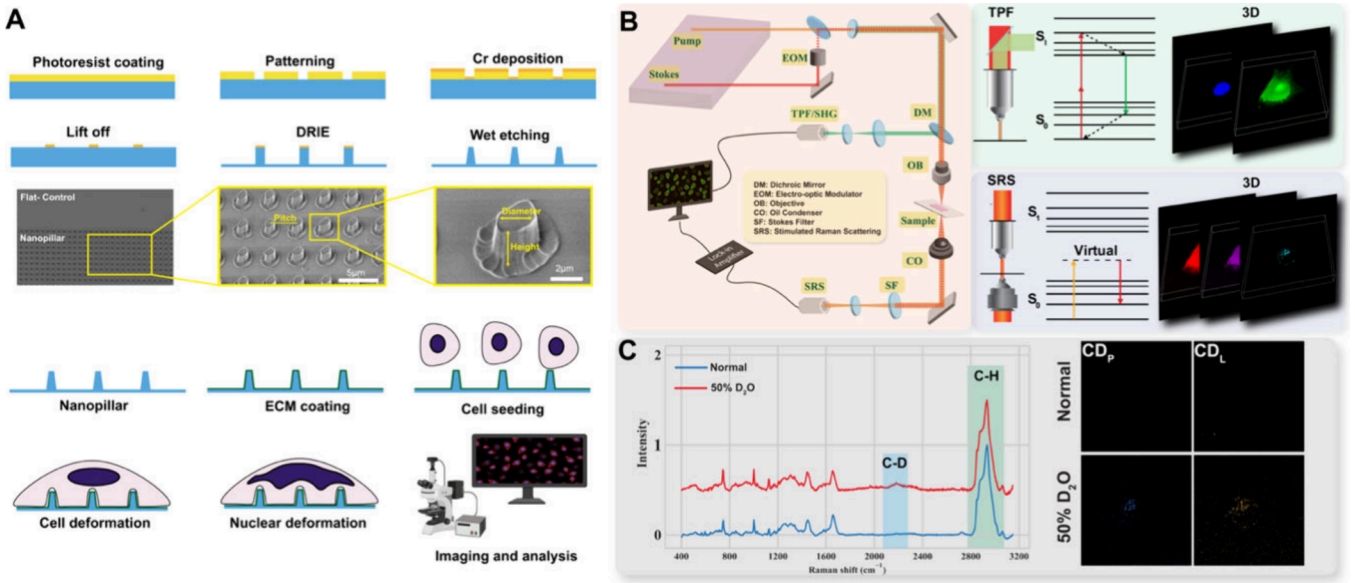

Figure 1. Fabrication and characterization of nanopillar arrays and a multimodal imaging setup. (A) Schematic illustration of the fabrication process of nanopillar arrays. Scanning electron microscopy (SEM) images showed the detailed structure of the nanopillars. Then, the nanopillars were coated with extracellular matrix (ECM) proteins, followed by cell seeding, leading to cell and nuclear deformation observable under microscopy. (B) Schematic figure of the multimodal optical imaging platform combining TPF and SRS enabled a 3D visualization of cells with high spatial resolution and imaging of various biomolecules. (C) Raman spectra of HeLa cells under normal and 50% heavy water (D_2O) conditions highlighting the shifts in carbon−hydrogen (C−H) and C−D chemical bonds. SRS images revealed the C−D signal shown in the 50% heavy water condition, allowing visualization of metabolic dynamics, including newly synthesized proteins and lipids.

detection of the stimulated Raman loss signal. The output current from the photodiode was terminated, filtered, and demodulated by a lock-in amplifier at 20 MHz. The demodulated signal was input into the FV3000 software module FV-OSR (Olympus) to generate image during laser scanning. All images obtained were 512 × 512 pixels with a dwell time 40 μs. The pixel size is 0.25 um x 0.25 um. Each image series typically contained 3−5 cells. We acquired 10−12 slices per image stack, with a step size of 1 um.

Image Segmentation

Before segmenting the images, all of the 3D image stacks were compressed into 2D images for better display by selecting the maximum intensity value along the *z*-axis for each x-y position. QuPath[36] was used to segment the cell cytoplasmic and nuclear regions based on the protein image for all of the quantitative analysis (Figure S2).

Multivariate Analysis

All analyses were based on the pixel values of ratiometric images. 20000 pixels were randomly chosen from cells on both flat and nanopillar surfaces, and the generated data sets were used as the input for the downstream analysis. Uniform Manifold Approximation and Projection (UMAP), pairwise scatter plot, and hierarchical cluster heatmap, and all of these data analysis pipelines were performed using home-built python scripts.

Statistical Analysis

All of the quantitative results are from images of 10−12 cells cultured on both flat and nanopillar substrates. One-way ANOVA tests were performed through Python and GraphPad Prism. A p-value <0.05 is considered statistically significant.

RESULTS AND DISCUSSION

Multimodal Imaging of Cells on Nanopillar Arrays

To study the effects of surface topography on cellular metabolism, we first fabricated the nanopillar arrays for the seeding of HeLa cells (Figure 1A). The process began with photoresist coating and patterning, followed by chromium deposition, lift-off, and deep reactive ion etching (DRIE). The process concluded with wet etching, which defined the nanopillar structures. These structures were then characterized using scanning electron microscopy (SEM) to confirm their precise architecture. Then, the nanopillar arrays were coated with ECM to enhance cell attachment and proliferation. The interaction of cells with these nanotopographies led to notable cellular and nuclear deformation.

To study the metabolism alternation induced by nanotopography, we employed a multimodal optical imaging platform (Figure 1B). In TPF imaging mode, laser beams at 781 and 860 nm were used to excite reduced nicotinamide adenine dinucleotide (NADH) and flavin adenine dinucleotide (FAD) molecules, respectively. In SRS imaging mode, a tunable pump laser beam (780−990 nm) and a fixed Stokes laser beam (1031 nm) were used to visualize different vibrational modes. Additionally, by incorporating 50% heavy water (D_2O) into the HeLa cell culture medium, we observed the metabolic dynamics of the cells. This was evidenced by the appearance of a new peak around 2100−2200 cm^{-1} in the Raman spectra of HeLa cells, compared to the normal condition without D_2O. This peak signified the formation of carbon-deuterium (C−D) chemical bonds in the newly synthesized biomolecules. Corresponding SRS images visualized newly synthesized proteins (CD_P) and lipids (CD_L), providing insights into metabolic activities in cells. Furthermore, our findings indicated that newly synthesized lipids (CD_L) were primarily localized on the basal regions of the cells (Figure S1). To capture these localized changes and provide a comprehensive analysis, we employed 3D imaging to study cellular metabolism in this study. For quantification and display purposes, each 2D image represents the maximum projection of the respective 3D image stack. By utilizing 3D imaging, we were able to visualize and analyze the nanopillar-induced alterations in cellular morphology and metabolism

https://doi.org/10.1021/cbmi.4c00051
Chem. Biomed. Imaging 2024, 2, 825−834

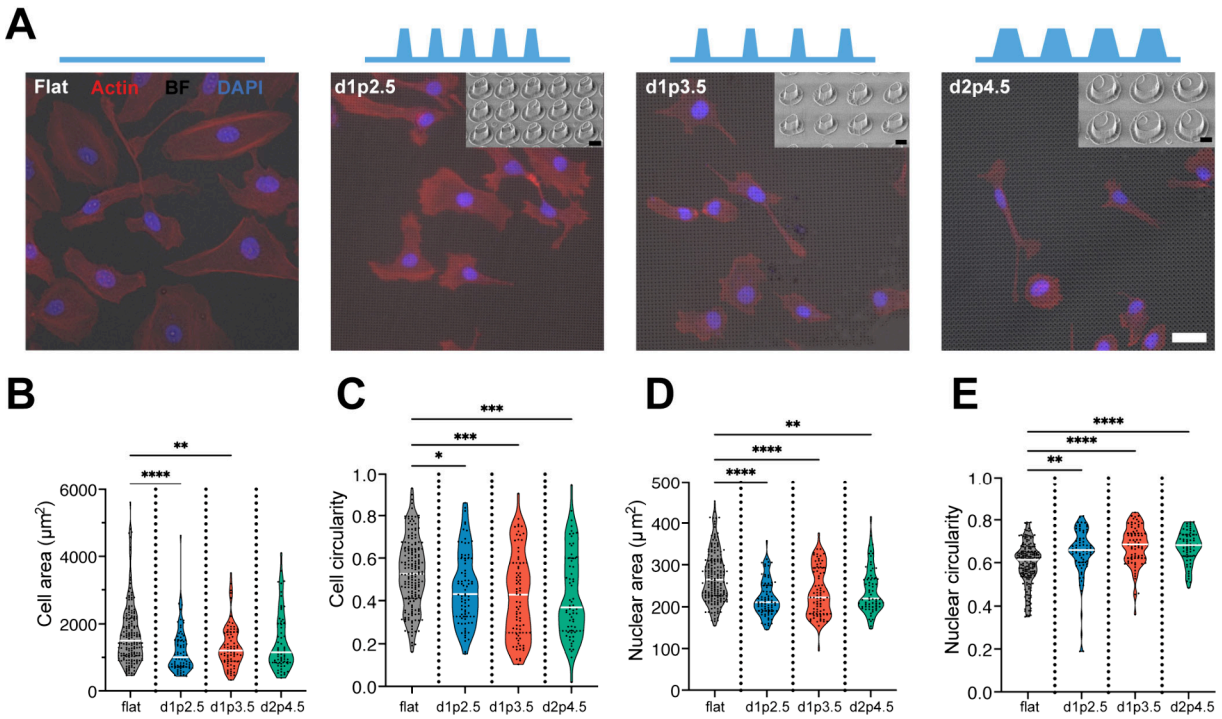

Figure 2. Morphological analysis of cells cultured on flat and nanopillar surfaces. (A) Cell area, (B) cell circularity, (C) nuclear area, and (D) nuclear circularity quantified for cells on flat surfaces and nanopillar surfaces with different diameter and pitch configurations: d1p2.5, d1p3.5, and d2p4.5. (E) Representative fluorescence microscopy images of cells stained for nuclei (blue) and actin (red) on flat and nanopillar surfaces. Statistical significance was determined using the one-way ANOVA test. *$p < 0.05$; **$p < 0.01$; ***$p < 0.001$; ****$p < 0.0001$. Scale bar, 40 μm. d1p2.5: diameter of nanopillar is 1 μm and the center-to-center pitch between nanopillars is 2.5 μm.

with improved accuracy and detail as compared to relying solely on 2D imaging.

Morphology Changes of Cells and Nuclei on Nanopillar Substrates

Fluorescent microscopy images and morphological analysis of cells stained with actin-phalloidin and nucleus (DAPI) on the nanopillar and flat surfaces showed that nanopillar sizes (pitch and diameter) significantly impacted the cell area, cell circularity, nuclear area, and nuclear circularity (Figure 2A).

We tested cells on various nanopillar configurations including d1p2.5 (diameter 1.058 ± 0.062 μm, center-to-center pitch 2.574 ± 0.184 μm, height= 1.552 ± 0.095 μm), d1p3.5(diameter 1.011 ± 0.065 μm, center-to-center pitch 3.565 ± 0.054 μm, height= 1.558 ± 0.080) and d2p4.5 (diameter 2.077 ± 0.062 μm, center-to-center pitch 4.558 ± 0.052 μm, height= 1.554 ± 0.056), and flat substrate as control. We have designated areas without nanopillars on the chip to use as the internal control to enable a direct comparison between flat and nanopillar regions (Figure 1A). The different pitch and diameter parameters tested in the study allowed for the investigation of the roles of surface topography on cellular and nuclear functions.

Cells on nanotopographies showed a smaller cellular area, with those cultured on d1p3.5 structures having the smallest area (1206 ± 690.2 μm^2), compared to those on flat surfaces (1710 ± 936.7 μm^2) (Figure 2B). This behavior aligned with previous research which claimed that cells on nanotopographies tend to have a smaller area.[17]

Cells on nanopillar surfaces showed lower circularity values, suggesting more deformation of cells with irregular shapes compared with those on the flat surface (0.53 ± 0.16; Figure 2C). This implies that nanopillar surfaces promoted cell elongation and cellular deformation due to the physical constraints imposed by the nanopillars.

The shape of the nucleus also followed cellular morphology, where cells on nanopillar surfaces had smaller nuclear areas, with those cultured on d1p2.5 having the smallest nuclear area (221.3 ± 44.25 μm^2), compared to those on flat surfaces (271.5 ± 61.45 μm^2) (Figure 2D).

Interestingly, nuclear circularity showed an opposite trend to that of cell circularity. Cells on nanopillar surfaces, such as d1p3.5 (0.68 ± 0.09), had higher nuclear circularity compared to those on flat surfaces (0.59 ± 0.09) (Figure 2E). This suggests that while the cell body became more irregular on nanopillar surfaces, the nucleus maintained a more regular shape, possibly due to the cytoskeletal support that was maintaining nuclear integrity.

These results highlight that such physical cues can impact cellular functions such as differentiation, gene expression, and metabolism that are crucial for cellular fate by changing cellular and nuclear morphology.[37,38]

Cell Metabolism Alteration by Nanopillar–Cell Interactions

Understanding cellular metabolism on engineered nanostructured surfaces is crucial for advancing biomedical applications. We investigated the effects of nanopillar substrates on cellular metabolic processes spatially and quantitatively, including the optical redox ratio, protein turnover, lipid turnover, and lipid unsaturation levels, through our multimodal optical imaging platform (Figure 3A).

FAD and NADH, functioning as electron carriers during cellular respiration, play a key role in cellular metabolism.[39] The optical redox ratio, defined as FAD/(FAD+NADH) ratio, is a crucial indicator of cellular oxidative stress and

https://doi.org/10.1021/cbmi.4c00051
Chem. Biomed. Imaging 2024, 2, 825−834

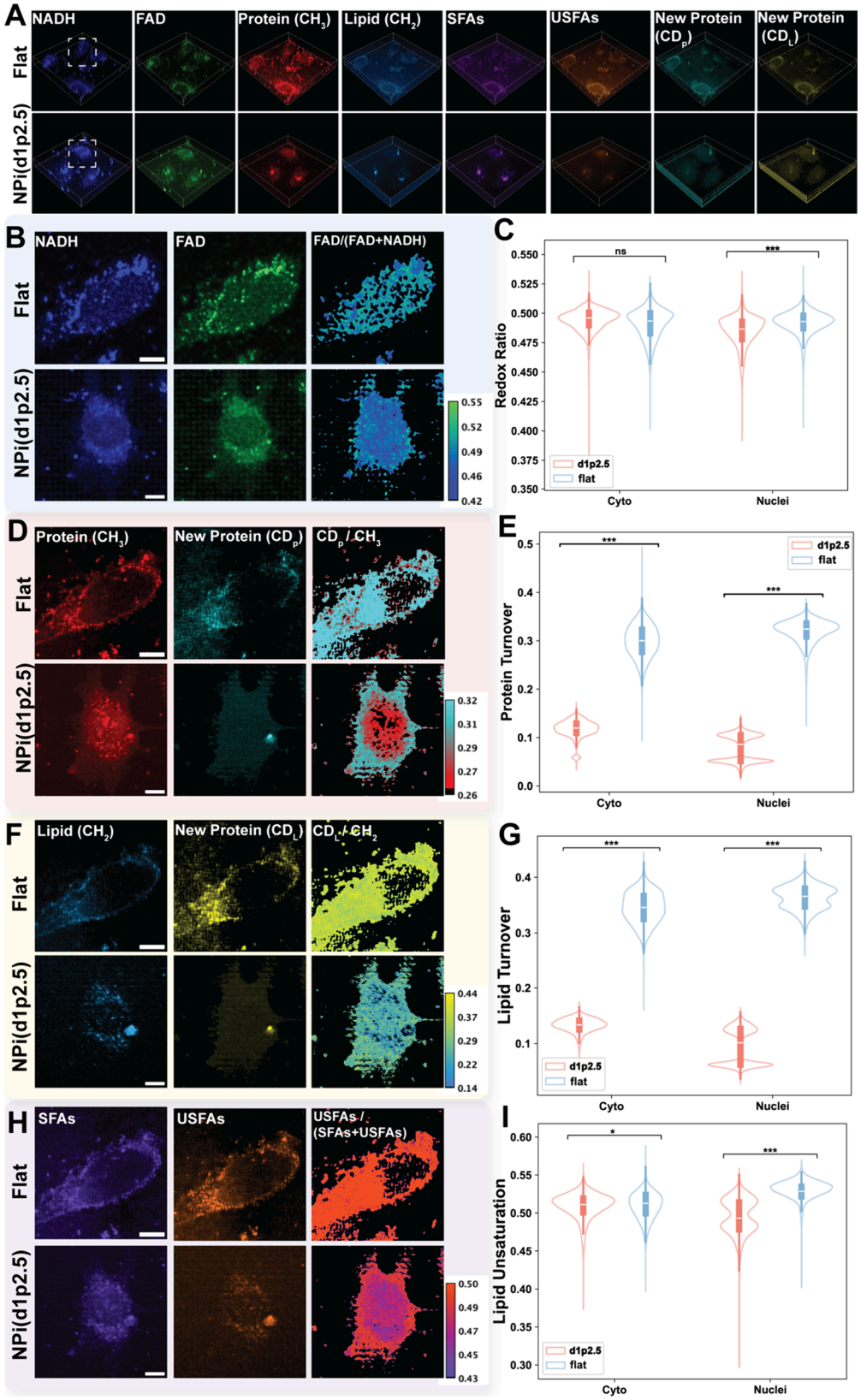

Figure 3. Multimodal imaging of metabolic activities of cells cultured on flat and nanopillar (d1p2.5) substrates. (A) 3D multimodal imaging of HeLa cells showing various metabolic markers on flat and nanopillar substrates, respectively. (B–H) Visualization of the optical redox ratio, protein turnover, lipid turnover, lipid unsaturation in cells on flat versus nanopillar surfaces, respectively. Protein turnover refers to the ratio of newly synthesized proteins (CD_P) to total protein (CH_P), and lipid turnover represents the ratio of newly synthesized lipids (CD_L) to pre-existing lipids (CH_L). (C, E, G, I) Quantitative analysis of optical redox ratio, protein turnover, lipid turnover, lipid unsaturation in cells on flat surfaces in contrast to nanopillar surfaces. The analysis included the segmentation of cytoplasmic and nuclear regions for comparison (n = 10 cells). Statistical significance was determined using the one-way ANOVA test. *p < 0.05; **p < 0.01; ***p < 0.001; ****p < 0.0001. Scale bar, 10 μm.

https://doi.org/10.1021/cbmi.4c00051
Chem. Biomed. Imaging 2024, 2, 825–834

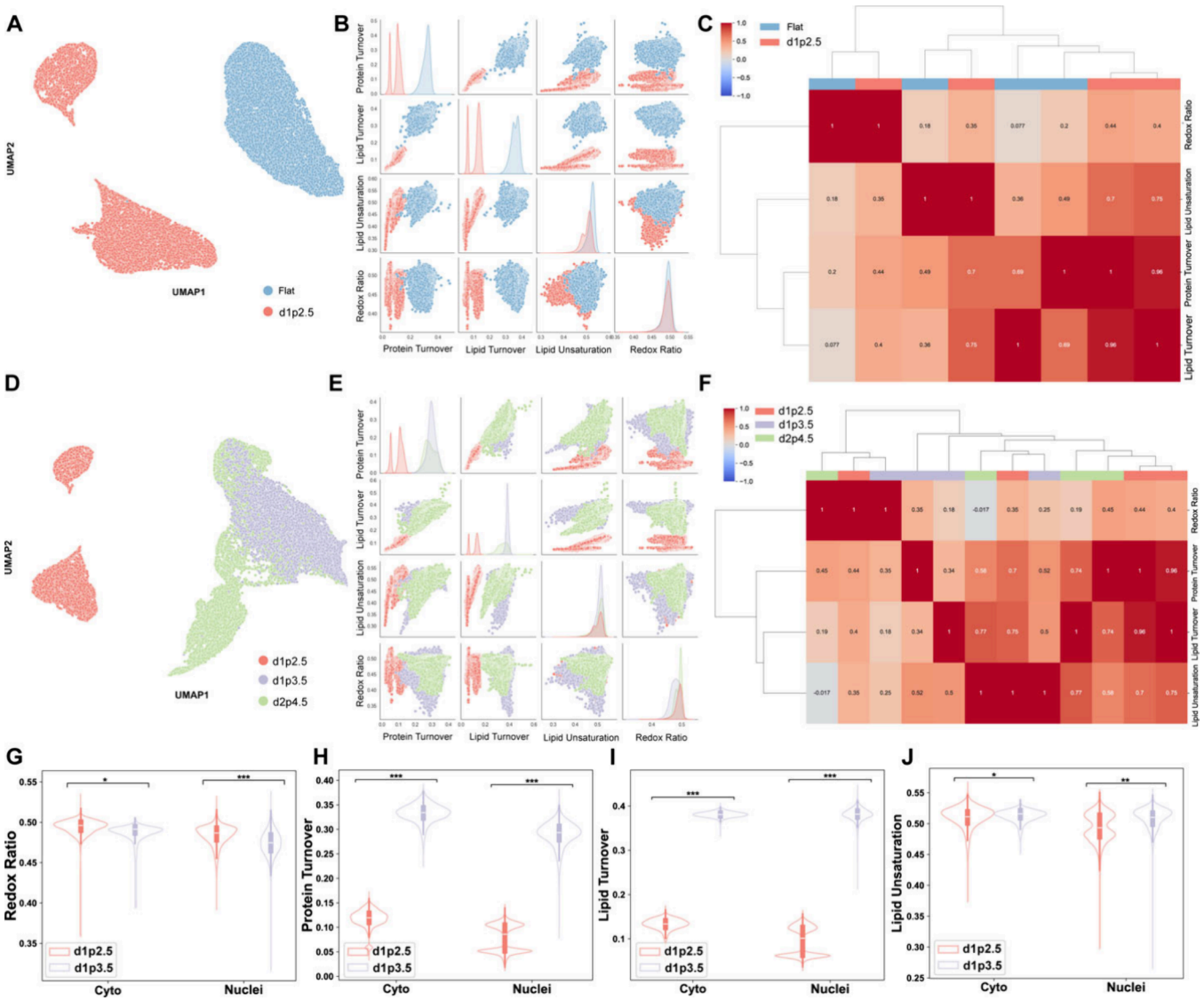

Figure 4. Multivariate analysis of metabolic profiles in cells cultured on flat and various nanopillar surfaces. (A) UMAP analysis of pixel clusters from cells on both flat (blue) and nanopillar (d1p2.5) surfaces (red). (B) Pairwise scatter plots of metabolic profiles of pixels including redox ratio, lipid unsaturation, protein turnover, and lipid turnover. (C) Hierarchical clustering heatmap of metabolic profiles for cells on flat and nanopillar (d1p2.5) surfaces. (D) UMAP analysis of pixel clusters from cells on different nanopillar configurations: d1p2.5 (red), d1p3.5 (purple), and d2p4.5 (green). (E) Pairwise scatter plots of metabolic profiles of pixels from cells across different nanopillar configurations. (F) Hierarchical clustering heatmap of metabolic features for cells on different nanopillar configurations (d1p2.5, d1p3.5, d2p4.5). (G–J) Violin plots in the redox ratio, protein turnover, lipid turnover and lipid unsaturation between cytoplasmic and nuclear regions for cells on nanopillar surfaces d1p2.5 and d1p3.5, respectively (n = 10 cells). Statistical significance is determined by using one-way ANOVA test. *p < 0.05; **p < 0.01; ***p < 0.001; ****p < 0.0001. d1p2.5: diameter of nanopillar is 1 μm and the pitch between nanopillars is 2.5 μm. d1p3.5: diameter of nanopillar is 1 μm and the pitch between nanopillars is 3.5 μm. d2p4.5: diameter of nanopillar is 2 μm and the pitch between nanopillars is 4.5 μm.

mitochondrial activity.[40] While typically optical redox ratio was associated with cytoplasmic and mitochondrial activities, it was known that the nucleus also contains FAD and NADH.[41,42] Recent studies characterized and compared the redox status between nuclear and cytoplasmic compartments of cancer cells to find the potential biomarkers for breast cancer aggressiveness.[43] By analyzing the ratiometric images of FAD/(FAD +NADH) (Figure 3B), we revealed that HeLa cells cultured on nanopillar arrays exhibited a relatively lower optical redox ratio in the nuclear regions compared to cells on flat substrates. There was no difference in the redox ratios in the cytoplasmic compartments between cells on different substrates. This shift suggested that the unique topographical features of nanopillars modulated mitochondrial function and redox homeostasis in cells. Moreover, these findings showed that nanopillar arrays increased the surface area with which cells interacted and created distinct mechanical environments, influencing intracellular signaling pathways that regulate oxidative stress responses. The quantitative results of the optical redox ratio (Figure 3C) further supported the notion that nanotopography reduces the metabolic activities within the cells.

To investigate the metabolic dynamics of lipids and protein in HeLa cells, we incorporated 50% D_2O into cells and used SRS imaging to detect the C–D bonds that represent newly synthesized biomolecules within the cells (Figure 3D, F). The protein and lipid turnover ratios of newly synthesized protein/lipids to pre-existing protein/lipids were significantly lower in cells cultured on nanopillar substrates, in both the nucleus and

https://doi.org/10.1021/cbmi.4c00051
Chem. Biomed. Imaging 2024, 2, 825–834

cytoplasm, compared to cells on flat surfaces (Figure 3E, G). This difference implies that mechanical cues from the nanopillars affected cellular signaling pathways involved in protein and lipid biosynthesis and degradation. The altered protein and lipid turnovers may have implications for cell growth, differentiation, and response to environmental stimuli. The mechanical stress triggered by nanopillar topography likely played a critical role in modulating these cellular processes, offering insights into how physical alterations from the extracellular environment influence cellular metabolic dynamics.

Lipid compositions are crucial for maintaining cell membrane fluidity and facilitating cellular signaling. Lipids with long saturated fatty acids can result in thicker, less elastic, and less fluid membranes because of the tighter packing. Unsaturated fatty acids do the opposite due to the kinked acyl chains[44] Recent research has shown that nontopographic materials can enable transient openings and breach the nucleo-cytoplasmic barrier.[45] The mechanical stress induced by the nanopillars likely affected lipid unsaturation level in cells because they changed the cells' physical properties. Figures 3H and 3I show decreased lipid unsaturation in cells on nanopillar substrates, potentially due to enhanced lipid desaturation processes. This adaptation helped balance changes in the cell membrane structure caused by the mechanical forces driven by the nanopillars. The spatial distribution and quantitative analysis between these metabolic changes highlighted the complex relationship between cellular metabolism and the physical properties of the nanopillar substrates. Nanopillar arrays not only altered the mechanical environment of cells but also influenced key metabolic pathways.

Multivariate Analysis of Metabolic Profiles

The intricacies of cellular metabolism are profoundly influenced by the physical characteristics of the substrate on which cells are cultured. To classify those cells based on their metabolic activities and uncover correlations between various metabolic features, we utilized multivariate analysis to explore the metabolic alterations of cells grown on nanopillar surfaces versus those on flat surfaces. Specifically, we randomly selected 20000 image pixels from 10 to 12 cells on both nanopillar (d1p2.5, d1p3.5, d2p4.5) and flat substrates, with four metabolic profiles for each pixel.

Notably, the UMAP (Uniform Manifold Approximation and Projection) analysis, a dimensionality reduction technique for visualizing high-dimensional data,[46] clearly distinguished cells cultured on nanopillar surfaces (d1p2.5) from those on flat surfaces according to their metabolic profiles (Figure 4A). This finding underscored the significant impact of nanotopography on cellular metabolism, independent of morphological visualization. Further examination through pairwise scatter plots revealed distinct distributions of values of key metabolic profiles (Figure 4B), emphasizing that the most significant metabolism differences for classifying cells on nanopillar arrays and flat surfaces were driven by the metabolic dynamics. Additionally, the hierarchical clustering heatmap demonstrated higher positive correlations between metabolic dynamics and redox ratio/lipid unsaturation in cells on nanopillars compared to those on flat surfaces (Figure 4C). The heatmap results indicated that the interactions between the cell and nanopillars could trigger interconnected metabolic activity alternations, such as changes in protein and lipid turnover, which in turn could significantly influence other metabolic profiles.

To delve deeper into how the geometry of nanotopography affects the cellular metabolism, we expanded our multivariate analysis to include different nanopillar configurations (d1p2.5, d1p3.5, and d2p4.5). We compared nanopillar arrays with the same diameter but different pitch parameters (d1p2.5 and d1p3.5), and those with different diameters but the same interpillar spacing (d1p3.5, d2p4.5). Interestingly, the UMAP analysis distinctly separated the d1p2.5 clusters from the other two configurations, while the d1p3.5 and d2p4.5 clusters converged into a localized region (Figure 4D). This result suggested that interpillar spacing played a more crucial role in modulating cellular metabolism than the diameter. It aligned with the hypothesis that increased spacing between nanopillars induces more substantial changes in cell morphology, subsequently altering the cellular metabolism. Pairwise scatter plots further clarified these differences by revealing exclusive metabolic profiles (Figure 4E). Hierarchical clustering heatmaps based on the similarities of various metabolic profiles cross different nanopillar configurations elucidated that cells on nanopillars with larger interpillar spacing (d1p3.5) had relatively lower correlation similarity between protein and lipid synthesis compared to those with smaller interpillar spacing (d1p2.5) (Figure 4F). Finally, a quantitative analysis of each metabolic profile between d1p2.5 and d1p3.5 revealed that larger interpillar spacing (d1p3.5) surfaces led to a lower redox ratio, higher protein and lipid syntheses, and higher lipid unsaturation (Figure 4G–J). These results underscored the specific metabolic alterations achieved by manipulating the geometry of nanopillars, particularly the interpillar spacing. The ability to fine-tune cellular metabolism through engineered nanotopographies offers valuable insights into designing advanced therapeutic strategies and biomaterial interfaces.

CONCLUSION

In this study, we utilized a novel multimodal optical imaging platform that integrates TPF and SRS microscopy to visualize and quantify cellular metabolic changes in response to engineered nanotopographies. Our multimodal technology's key innovation of our multimodal technology was the integration of two-photon fluorescence (TPF) and stimulated Raman scattering (SRS) microscopy into a single, uniformed platform. This platform allows for visualizing multiple molecular and cellular features at the same region of interest. Our results revealed that nanopillars not only altered cellular and nuclear morphologies but also significantly influenced cellular metabolic activities. Specifically, nanopillars led to relatively lower oxidative stress and lipid unsaturation within cells along with significantly reduced protein and lipid syntheses. These alternations could be attributed to the physical constraints imposed by nanopillars through mechano-transduction mechanisms.[47] Nanopillars likely created local areas of high curvature on the cell membrane potentially leading to clustering of mechanosensitive proteins such as integrins.[48] This clustering would activate various signaling cascades to influence the cytoskeleton organization and cellular metabolism. Furthermore, the nuclear deformation observed in our study might lead to changes of chromatin organization, potentially affecting gene expressions related to metabolic processes.[49] The reduced oxidative stress that we observed in cells on nanopillars could be a result of mitochondrial dynamics or activation of antioxidant pathways in response to mechanical stress. Additionally, the decreased protein and

https://doi.org/10.1021/cbmi.4c00051
Chem. Biomed. Imaging 2024, 2, 825−834

lipid syntheses could be linked to AMPK signaling pathways activated by nanotopography-induced mechanical stress.[50] By applying the multivariate analysis technique, we identified metabolic differences between cells on nanopillars and those on flat substrates. Notably, we observed that the geometry of the nanopillars, particularly the interpillar spacing, had a notable impact on cellular metabolic alterations, offering deeper insights into modulating cellular metabolism via engineered nanotopographies.[50] Using hierarchical clustering heatmaps, we captured cluster similarities and correlations among various metabolic profiles, further elucidating the interconnectedness of metabolic changes within cells.

Overall, these findings highlighted that the physical microenvironment manipulation by the nanopillars induced metabolic reprogramming in cells, which provided crucial insights into how nanotopographies can be engineered to modulate cellular metabolism and offer new possibilities for biomedical applications. For instance, in drug delivery systems, understanding how cells interact with and respond metabolically to nanostructures could inform the design of more effective nanocarriers, potentially improving drug uptake and efficacy. For regenerative medicine strategies, engineered scaffolds with defined nanotopographies could be created to guide tissue formation by controlling cell metabolism, potentially enhancing the success of tissue engineering approaches. Moreover, the observed changes in lipid metabolism and membrane properties on nanopillar substrates could inform the development of new strategies for manipulating cell membrane permeability with potential applications in drug delivery and cell-based therapies.

From those nanopillar configurations tested in our study, we revealed that controlling the interpillar space can cause more significant effects on cell metabolism compared to nanopillar diameter. However, to fully understand and harness these effects, a wider range of nanopillar configurations need to be tested for more precise and effective manipulation of cell metabolism through nanotopographies.

■ ASSOCIATED CONTENT

Data Availability Statement

All data generated or analyzed during this study are available upon request.

Supporting Information

The Supporting Information is available free of charge at https://pubs.acs.org/doi/10.1021/cbmi.4c00051.

3D multimodal metabolic images of HeLa cells on different nanopillar arrays; protein channel SRS image of HeLa cells and its segmented image for quantification (PDF)

■ AUTHOR INFORMATION

Corresponding Authors

Zeinab Jahed − *Shu Chien-Gene Lay Department of Bioengineering and Aiiso Yufeng Li Family Department of Chemical and Nano Engineering, University of California San Diego, La Jolla, California 92093, United States*; Email: zjahed@ucsd.edu

Lingyan Shi − *Shu Chien-Gene Lay Department of Bioengineering, Aiiso Yufeng Li Family Department of Chemical and Nano Engineering, Electrical and Computer Engineering, Institute of Engineering in Medicine, and Synthetic Biology Institute, University of California San Diego, La Jolla, California 92093, United States*; orcid.org/0000-0003-1373-3206; Email: l2shi@ucsd.edu

Authors

Zhi Li − *Shu Chien-Gene Lay Department of Bioengineering, University of California San Diego, La Jolla, California 92093, United States*; orcid.org/0009-0008-0675-5494

Einollah Sarikhani − *Aiiso Yufeng Li Family Department of Chemical and Nano Engineering, University of California San Diego, La Jolla, California 92093, United States*; orcid.org/0000-0002-7841-5244

Sirasit Prayotamornkul − *Shu Chien-Gene Lay Department of Bioengineering, University of California San Diego, La Jolla, California 92093, United States*; orcid.org/0009-0002-5170-6970

Dhivya Pushpa Meganathan − *Shu Chien-Gene Lay Department of Bioengineering, University of California San Diego, La Jolla, California 92093, United States*

Complete contact information is available at: https://pubs.acs.org/10.1021/cbmi.4c00051

Author Contributions

#Z.L. and E.S. contributed equally to this work. Z.L.: Conceptualization, Methodology, Investigation, Formal analysis, Visualization; Writing−original draft; Writing−review and editing). E.S.: Conceptualization, Methodology, Investigation, Formal analysis, Visualization; Writing−original draft; Writing−review and editing). D.P.M.: Investigation. Z.J.: Conceptualization, Methodology, Validation, Resources, Supervision; Writing−original draft, Writing−review and editing). L.S.: Conceptualization, Methodology, Validation, Resources, Supervision, Writing−original draft, Writing−review and editing.

Notes

The authors declare no competing financial interest.

■ ACKNOWLEDGMENTS

This work was performed in part at the San Diego Nanotechnology Infrastructure (SDNI) of UCSD, a member of the National Nanotechnology Coordinated Infrastructure, which is supported by the National Science Foundation (Grant ECCS-2025752). This work was in part supported by Air Force Office of Scientific Research YIP award (AFOSR FA9550-23-1-0090) and Cancer research coordinating committee faculty seed grant to Z.J. We acknowledge support from NIH R01GM149976, NIH U01AI167892, NIH 5R01NS111039, NIH R21NS125395, U54CA132378, Sloan Research Fellow Award, and Hellman Fellow Award.

■ REFERENCES

(1) Ermis, M.; Antmen, E.; Hasirci, V. Micro and Nanofabrication methods to control cell-substrate interactions and cell behavior: A review from the tissue engineering perspective. *Bioactive materials* **2018**, *3* (3), 355−369.

(2) Skoog, S. A.; Kumar, G.; Narayan, R. J.; Goering, P. L. Biological responses to immobilized microscale and nanoscale surface topographies. *Pharmacology & therapeutics* **2018**, *182*, 33−55.

(3) Hansel, C. S.; Crowder, S. W.; Cooper, S.; Gopal, S.; João Pardelha da Cruz, M.; de Oliveira Martins, L.; Keller, D.; Rothery, S.; Becce, M.; Cass, A. E.; et al. Nanoneedle-mediated stimulation of cell

mechanotransduction machinery. *ACS Nano* **2019**, *13* (3), 2913−2926.
(4) Elnathan, R.; Tay, A.; Voelcker, N. H.; Chiappini, C. The start-ups taking nanoneedles into the clinic. *Nat. Nanotechnol.* **2022**, *17* (8), 807−811.
(5) Murphy, W. L.; McDevitt, T. C.; Engler, A. J. Materials as stem cell regulators. *Nature materials* **2014**, *13* (6), 547−557.
(6) Finbloom, J. A.; Huynh, C.; Huang, X.; Desai, T. A. Bioinspired nanotopographical design of drug delivery systems. *Nature Reviews Bioengineering* **2023**, *1* (2), 139−152.
(7) Qiu, J.; Zhao, H.; Lei, Y. Emerging smart design of electrodes for micro-supercapacitors: A review. *SmartMat* **2022**, *3* (3), 447−473.
(8) Sarikhani, E.; Pushpa Meganathan, D.; Rahmani, K.; Tsai, C.-T.; Marquez-Serrano, A.; Li, X.; Santoro, F.; Cui, B.; Hyldgaard Klausen, L.; Jahed, Z. Engineering cell and nuclear morphology on nano topography by contact-free protein micropatterning. *bioRxiv*, 2023, 2023.06.05.543791
(9) Hanson, L.; Zhao, W.; Lou, H.-Y.; Lin, Z. C.; Lee, S. W.; Chowdary, P.; Cui, Y.; Cui, B. Vertical nanopillars for in situ probing of nuclear mechanics in adherent cells. *Nature Nanotechnol.* **2015**, *10* (6), 554−562.
(10) Losero, E.; Jagannath, S.; Pezzoli, M.; Goblot, V.; Babashah, H.; Lashuel, H. A.; Galland, C.; Quack, N. Neuronal growth on high-aspect-ratio diamond nanopillar arrays for biosensing applications. *Sci. Rep.* **2023**, *13* (1), 5909.
(11) Jahed, Z.; Yang, Y.; Tsai, C.-T.; Foster, E. P.; McGuire, A. F.; Yang, H.; Liu, A.; Forro, C.; Yan, Z.; Jiang, X.; et al. Nanocrown electrodes for parallel and robust intracellular recording of cardiomyocytes. *Nat. Commun.* **2022**, *13* (1), 2253.
(12) Zhang, A.; Lieber, C. M. Nano-bioelectronics. *Chem. Rev.* **2016**, *116* (1), 215−257.
(13) Lin, Z. C.; Xie, C.; Osakada, Y.; Cui, Y.; Cui, B. Iridium oxide nanotube electrodes for sensitive and prolonged intracellular measurement of action potentials. *Nat. Commun.* **2014**, *5* (1), 3206.
(14) Zeng, Y.; Zhuang, Y.; Vinod, B.; Guo, X.; Mitra, A.; Chen, P.; Saggio, I.; Shivashankar, G.; Gao, W.; Zhao, W. Guiding irregular nuclear morphology on nanopillar arrays for malignancy differentiation in tumor cells. *Nano Lett.* **2022**, *22* (18), 7724−7733.
(15) Li, X.; Klausen, L. H.; Zhang, W.; Jahed, Z.; Tsai, C.-T.; Li, T. L.; Cui, B. Nanoscale surface topography reduces focal adhesions and cell stiffness by enhancing integrin endocytosis. *Nano Lett.* **2021**, *21* (19), 8518−8526.
(16) Zhou, J.; Zhang, X.; Sun, J.; Dang, Z.; Li, J.; Li, X.; Chen, T. The effects of surface topography of nanostructure arrays on cell adhesion. *Phys. Chem. Chem. Phys.* **2018**, *20* (35), 22946−22951.
(17) Wang, K.; Man, K.; Liu, J.; Meckes, B.; Yang, Y. Dissecting physical and biochemical effects in nanotopographical regulation of cell behavior. *ACS Nano* **2023**, *17* (3), 2124−2133.
(18) Yang, L.; Jurczak, K. M.; Ge, L.; van Rijn, P. High-throughput screening and hierarchical topography-mediated neural differentiation of mesenchymal stem cells. *Adv. Healthcare Mater.* **2020**, *9* (11), 2000117.
(19) Lestrell, E.; Chen, Y.; Aslanoglou, S.; O'Brien, C. M.; Elnathan, R.; Voelcker, N. H. Silicon Nanoneedle-Induced Nuclear deformation: implications for human somatic and stem cell nuclear mechanics. *ACS Appl. Mater. Interfaces* **2022**, *14* (40), 45124−45136.
(20) Ramos, A. P.; Cruz, M. A.; Tovani, C. B.; Ciancaglini, P. Biomedical applications of nanotechnology. *Biophysical reviews* **2017**, *9* (2), 79−89.
(21) Villanueva-Flores, F.; Castro-Lugo, A.; Ramírez, O. T.; Palomares, L. A. Understanding cellular interactions with nanomaterials: Towards a rational design of medical nanodevices. *Nanotechnology* **2020**, *31* (13), 132002.
(22) Ramburrun, P.; Khan, R. A.; Choonara, Y. E. Design, preparation, and functionalization of nanobiomaterials for enhanced efficacy in current and future biomedical applications. *Nanotechnol. Rev.* **2022**, *11* (1), 1802−1826.
(23) Liu, R.; Liu, Q.; Pan, Z.; Liu, X.; Ding, J. Cell type and nuclear size dependence of the nuclear deformation of cells on a micropillar array. *Langmuir* **2019**, *35* (23), 7469−7477.
(24) Wakhloo, N. T. Deformability of cancer cells on 3D microstructured surfaces. Université de Haute Alsace-Mulhouse, 2018.
(25) Vargason, A. M.; Anselmo, A. C.; Mitragotri, S. The evolution of commercial drug delivery technologies. *Nature biomedical engineering* **2021**, *5* (9), 951−967.
(26) Li, Z.; Nguyen, C.; Jang, H.; Hoang, D.; Min, S.; Ackerstaff, E.; Koutcher, J. A.; Shi, L. Multimodal imaging of metabolic activities for distinguishing subtypes of breast cancer. *Biomedical Optics Express* **2023**, *14* (11), 5764−5780.
(27) Fung, A. A.; Hoang, K.; Zha, H.; Chen, D.; Zhang, W.; Shi, L. Imaging sub-cellular methionine and insulin interplay in triple negative breast cancer lipid droplet metabolism. *Frontiers in Oncology* **2022**, *12*, 858017.
(28) Helmchen, F.; Denk, W. Deep tissue two-photon microscopy. *Nat. Methods* **2005**, *2* (12), 932−940.
(29) Griffiths, V. A.; Valera, A. M.; Lau, J. Y.; Roš, H.; Younts, T. J.; Marin, B.; Baragli, C.; Coyle, D.; Evans, G. J.; Konstantinou, G.; et al. Real-time 3D movement correction for two-photon imaging in behaving animals. *Nat. Methods* **2020**, *17* (7), 741−748.
(30) Freudiger, C. W.; Min, W.; Saar, B. G.; Lu, S.; Holtom, G. R.; He, C.; Tsai, J. C.; Kang, J. X.; Xie, X. S. Label-free biomedical imaging with high sensitivity by stimulated Raman scattering microscopy. *Science* **2008**, *322* (5909), 1857−1861.
(31) Wei, M.; Shi, L.; Shen, Y.; Zhao, Z.; Guzman, A.; Kaufman, L. J.; Wei, L.; Min, W. Volumetric chemical imaging by clearing-enhanced stimulated Raman scattering microscopy. *Proc. Natl. Acad. Sci. U. S. A.* **2019**, *116* (14), 6608−6617.
(32) Wei, L.; Chen, Z.; Shi, L.; Long, R.; Anzalone, A. V.; Zhang, L.; Hu, F.; Yuste, R.; Cornish, V. W.; Min, W. Super-multiplex vibrational imaging. *Nature* **2017**, *544* (7651), 465−470.
(33) Shi, L.; Zheng, C.; Shen, Y.; Chen, Z.; Silveira, E. S.; Zhang, L.; Wei, M.; Liu, C.; de Sena-Tomas, C.; Targoff, K. Optical imaging of metabolic dynamics in animals. *Nat. Commun.* **2018**, *9* (1), 2995.
(34) Sarikhani, E.; Meganathan, D. P.; Larsen, A.-K. K.; Rahmani, K.; Tsai, C.-T.; Lu, C.-H.; Marquez-Serrano, A.; Sadr, L.; Li, X.; Dong, M.; Santoro, F.; Cui, B.; Klausen, L. H.; Jahed, Z. Engineering the Cellular Microenvironment: Integrating Three-Dimensional Nontopographical and Two-Dimensional Biochemical Cues for Precise Control of Cellular Behavior. *ACS Nano* **2024**, *18* (29), 19064−19076.
(35) Sarikhani, E.; Patel, V.; Li, Z.; Meganathan, D. P.; Rahmani, K.; Sadr, L.; Hosseini, R.; Visda, D.; Shukla, S.; Naghsh-Nilchi, H.; Balaji, A.; McMahon, G.; Chen, S.; Schoneberg, J.; McHugh, C. A.; Shi, L.; Jahed, Z. Engineered Nanotopographies Induce Transient Openings in the Nuclear Membrane. *Adv. Funct. Mater.* **2024**, 2410035.
(36) Bankhead, P.; Loughrey, M. B.; Fernández, J. A.; Dombrowski, Y.; McArt, D. G.; Dunne, P. D.; McQuaid, S.; Gray, R. T.; Murray, L. J.; Coleman, H. G.; et al. QuPath: Open source software for digital pathology image analysis. *Sci. Rep.* **2017**, *7* (1), 1−7.
(37) Guilak, F.; Cohen, D. M.; Estes, B. T.; Gimble, J. M.; Liedtke, W.; Chen, C. S. Control of stem cell fate by physical interactions with the extracellular matrix. *Cell stem cell* **2009**, *5* (1), 17−26.
(38) Perestrelo, T.; Correia, M.; Ramalho-Santos, J.; Wirtz, D. Metabolic and mechanical cues regulating pluripotent stem cell fate. *Trends in cell biology* **2018**, *28* (12), 1014−1029.
(39) Chakraborty, S.; Nian, F.-S.; Tsai, J.-W.; Karmenyan, A.; Chiou, A.; et al. Quantification of the metabolic state in cell-model of Parkinson's disease by fluorescence lifetime imaging microscopy. *Sci. Rep.* **2016**, *6* (1), 1−9.
(40) Hu, L.; Wang, N.; Cardona, E.; Walsh, A. J. Fluorescence intensity and lifetime redox ratios detect metabolic perturbations in T cells. *Biomedical Optics Express* **2020**, *11* (10), 5674−5688.
(41) Heikal, A. A. Intracellular coenzymes as natural biomarkers for metabolic activities and mitochondrial anomalies. *Biomarkers in medicine* **2010**, *4* (2), 241−263.

(42) Wright, B. K.; Andrews, L. M.; Jones, M. R.; Stringari, C.; Digman, M. A.; Gratton, E. Phasor-FLIM analysis of NADH distribution and localization in the nucleus of live progenitor myoblast cells. *Microscopy research and technique* **2012**, *75* (12), 1717−1722.
(43) Jacob, A.; Xu, H. N.; Stout, A. L.; Li, L. Z. Subcellular analysis of nuclear and cytoplasmic redox indices differentiates breast cancer cell subtypes better than nuclear-to-cytoplasmic area ratio. *Journal of Biomedical Optics* **2022**, *27* (8), 086001−086001.
(44) Baccouch, R.; Shi, Y.; Vernay, E.; Mathelié-Guinlet, M.; Taib-Maamar, N.; Villette, S.; Feuillie, C.; Rascol, E.; Nuss, P.; Lecomte, S.; et al. The impact of lipid polyunsaturation on the physical and mechanical properties of lipid membranes. *Biochimica et Biophysica Acta (BBA)-Biomembranes* **2023**, *1865* (2), 184084.
(45) Sarikhani, E.; Patel, V.; Li, Z.; Meganathan, D. P.; Rahmani, K.; Sadr, L.; Hosseini, R.; Visda, D.; Shukla, S.; Naghsh-Nilchi, H.; et al. Engineered Nanotopographies Induce Transient Openings in the Nuclear Membrane. *Adv. Funct. Mater.* **2024**, 2410035.
(46) McInnes, L.; Healy, J.; Melville, J., Umap: Uniform manifold approximation and projection for dimension reduction. *arXiv*, 2018, 1802.03426.
(47) Hoffman, B. D.; Grashoff, C.; Schwartz, M. A. Dynamic molecular processes mediate cellular mechanotransduction. *Nature* **2011**, *475* (7356), 316−323.
(48) Zhang, W.; Lu, C.-H.; Nakamoto, M. L.; Tsai, C.-T.; Roy, A. R.; Lee, C. E.; Yang, Y.; Jahed, Z.; Li, X.; Cui, B. Curved adhesions mediate cell attachment to soft matrix fibres in three dimensions. *Nat. Cell Biol.* **2023**, *25* (10), 1453−1464.
(49) Dupont, S.; Wickström, S. A. Mechanical regulation of chromatin and transcription. *Nat. Rev. Genet.* **2022**, *23* (10), 624−643.
(50) Romani, P.; Brian, I.; Santinon, G.; Pocaterra, A.; Audano, M.; Pedretti, S.; Mathieu, S.; Forcato, M.; Bicciato, S.; Manneville, J.-B.; et al. Extracellular matrix mechanical cues regulate lipid metabolism through Lipin-1 and SREBP. *Nature cell biology* **2019**, *21* (3), 338−347.

https://doi.org/10.1021/cbmi.4c00051
Chem. Biomed. Imaging 2024, 2, 825−834